

Three-dimensional Configuration of Induced Magnetic Fields around Mars

Chi Zhang¹, Zhaojin Rong¹, Lucy Klinger², Hans Nilsson³, Zhen Shi⁴, Fei He⁵, Jiawei Gao⁶, Xinzhou Li⁵, Yoshifumi Futaana³, Robin Ramstad⁷, Xiao-Dong Wang³, Mats Holmström³, Stas Barabash³, Kai Fan⁸, and Yong Wei⁵

¹Key Laboratory of Earth and Planetary Physics, Institute of Geology and Geophysics, Chinese Academy of Sciences

²Beijing International Center for Mathematical Research, Peking University, China

³Swedish Institute of Space Physics

⁴IGGCAS

⁵Institute of Geology and Geophysics, Chinese Academy of Sciences

⁶GFZ German Research Center for Geosciences

⁷University of Colorado Boulder

⁸Institute of Geology and Geophysics Chinese Academy of Sciences

November 23, 2022

Abstract

Using over 6 years of magnetic field data (2014.10-2020.12) collected by the Mars Atmosphere and Volatile Evolution (MAVEN), we conduct a statistical study on the three-dimensional average magnetic field structure around Mars. We find that this magnetic field structure conforms to the pattern typical of an induced magnetosphere, that is, the interplanetary magnetic field (IMF) which is carried by the solar wind and which drapes, piles up, slips around the planet, and eventually forms a tail in the wake. The draped field lines from both hemispheres along the direction of the solar wind electric field (E) are directed towards the nightside magnetic equatorial plane, which looks like they are “sinking” toward the wake. These “sinking” field lines from the $+E$ -hemisphere (E pointing away from the plane) are more flared and dominant in the tail, while the field lines from the $-E$ -hemisphere (E pointing towards) are more stretched and “pinched” towards the plasma sheet. Such highly “pinched” field lines even form a loop over the pole of the $-E$ -hemisphere. The tail current sheet also shows an E -asymmetry: the sheet is thicker with a stronger tailward $J \times B$ force at $+E$ -flank, but much thinner and with a weaker $J \times B$ (even turns sunward) at $-E$ -flank. Additionally, we find that IMF B_x can induce a kink-like field structure at the boundary layer; the field strength is globally enhanced and the field lines flare less during high dynamic pressure; however, the rotation of the planet, against expectations, modulate the configuration of the tail current sheet insignificantly.

Three-dimensional Configuration of Induced Magnetic Fields around Mars

Chi Zhang^{1,2,3}, Zhaojin Rong^{1,2,4}, Lucy Klinger⁵, Hans Nilsson³, Zhen Shi^{1,2}, Fei He^{1,2}, Jiawei Gao^{1,2}, Xinzhou Li^{1,2}, Yoshifumi Futaana³, Robin Ramstad⁶, Xiaodong Wang³, Mats Holmström³, Stats Barabash³, Kai Fan^{1,2}, and Yong Wei^{1,2,4}

¹Key Laboratory of Earth and Planetary Physics, Institute of Geology and Geophysics, Chinese Academy of Sciences, Beijing, China

²College of Earth and Planetary Sciences, University of Chinese Academy of Sciences, Beijing, China

³Swedish Institute of Space Physics, Kiruna, Sweden

⁴Mohe Observatory of Geophysics, Beijing National Observatory of Space Environment, Institute of Geology and Geophysics, Chinese Academy of Sciences, Beijing, China

⁵Beijing International Center for Mathematical Research, Peking University, Beijing, China

⁶Laboratory for Atmospheric and Space Physics, University of Colorado, Boulder, CO, USA

***Corresponding author:** Zhaojin Rong (rongzhaojin@mail.iggcas.ac.cn)

Key Points:

- The magnetic field structure has an evident hemispheric asymmetry along the direction of the solar wind electric field.
- The tail current sheet is thicker and has a stronger tailward $\mathbf{J} \times \mathbf{B}$ force near the flank of the +E-hemisphere.
- The effects of IMF B_x , the dynamic pressure of solar wind, and the rotation of the planet on the field structure are surveyed respectively.

29 Abstract

30 Using over 6 years of magnetic field data (2014.10-2020.12) collected by the Mars
31 Atmosphere and Volatile Evolution (MAVEN), we conduct a statistical study on the three-
32 dimensional average magnetic field structure around Mars. We find that this magnetic field
33 structure conforms to the pattern typical of an induced magnetosphere, that is, the interplanetary
34 magnetic field (IMF) which is carried by the solar wind and which drapes, piles up, slips around
35 the planet, and eventually forms a tail in the wake. The draped field lines from both hemispheres
36 along the direction of the solar wind electric field (\mathbf{E}) are directed towards the nightside
37 magnetic equatorial plane, which looks like they are “sinking” toward the wake. These “sinking”
38 field lines from the +E-hemisphere (\mathbf{E} pointing away from the plane) are more flared and
39 dominant in the tail, while the field lines from the -E-hemisphere (\mathbf{E} pointing towards) are more
40 stretched and “pinched” towards the plasma sheet. Such highly “pinched” field lines even form a
41 loop over the pole of the -E-hemisphere. The tail current sheet also shows an E-asymmetry: the
42 sheet is thicker with a stronger tailward $\mathbf{J} \times \mathbf{B}$ force at +E-flank, but much thinner and with a
43 weaker $\mathbf{J} \times \mathbf{B}$ (even turns sunward) at -E-flank. Additionally, we find that IMF B_x can induce a
44 kink-like field structure at the boundary layer; the field strength is globally enhanced and the
45 field lines flare less during high dynamic pressure; however, the rotation of the planet, against
46 expectations, modulate the configuration of the tail current sheet insignificantly.

47

48 Plain Language Summary

49 To clarify the global magnetic field structure around Mars, we comprehensively study the
50 three-dimensional (3D) magnetic field structure of the Martian magnetosphere based on
51 measurements from MAVEN. Our study derives 3D distribution features of the magnetic field
52 structure, quantitatively estimates the tail current sheet and also investigates possible effects
53 brought by the IMF B_x , the dynamic pressure of solar wind, and planetary rotation on the
54 magnetic field structure. This 3D magnetic field structure around Mars is essential to
55 understanding the dynamic processes of the Martian magnetosphere.

56 **1 Introduction**

57 It is well known that both Venus and Mars lack a global dipole field and that the solar wind
58 plasma flow along with the “frozen-in” interplanetary magnetic field (IMF) interacts with the
59 atmosphere/ionosphere of the planet directly, resulting in an induced magnetosphere. On the
60 dayside, IMF piles up to form a magnetic barrier and drapes around the planet. The draped IMF
61 is stretched by the solar wind and slips into the wake to form an elongated induced magnetotail
62 [e.g., Acuña et al., 1998; Luhmann et al., 2004; Ma et al., 2002; McComas et al., 1986].
63 Researchers realize that most of the planetary ions escape to interplanetary space via the
64 electromagnetic force, e.g. the solar wind electric fields (E), the hall electric fields, and the
65 ambipolar electric fields [e.g., Barabash et al., 2007; Dubinin et al., 2011; Lundin, 2011; Dubinin
66 & Fraenz, 2015; Fang et al., 2010; Futaana et al., 2017; Nilsson et al., 2021; Zhang et al., 2021];
67 therefore, knowledge of the magnetic field structure around the Mars is vital for understanding
68 associated magnetospheric processes (e.g., the escape of planetary ions).

69 Venus is an ideal natural laboratory for studying an induced magnetosphere because the
70 planet has no significant intrinsic field and only relies on its ionosphere as an obstacle to solar
71 wind. Early studies based on the Pioneer Venus Orbiter have found a structure of draped field
72 lines in the distant downstream tail (8-12 Venusian radii) and demonstrated that there is an
73 asymmetrical tail field structure along the direction of the solar wind electric field (E -asymmetry)
74 [Saunders and Russell, 1986; McComas et al., 1986]. Studies based on observations of the Venus
75 Express, the ESA’s first mission to Venus [Titov et al., 2006], demonstrated that E -asymmetry
76 had already occurred in the terminator and the near-Venus tail, suggesting that magnetic field
77 lines are likely wrapped more tightly around Venus in the $-E$ -hemisphere (electric field points
78 towards planet) [Zhang et al., 2010; Du et al., 2013]. Rong et al. [2014] reconstructed the three-
79 dimensional (3-D) field structures of the near-Venus tail and found that its draped field lines
80 would sink into the wake, while the magnetic field structure of the tail current sheet would
81 become irregular in the $-E$ -hemisphere. Chai et al. [2016] suggested that a global looping field
82 around the tail might occur in addition to the draped field lines.

83 Unlike the induced magnetosphere of Venus, Mars has patches of localized intense remnant
84 crustal fields, particularly in the southern hemisphere [e.g., Acuña et al., 1999; Connerney et al.,
85 2005]. These crustal fields contribute to solar wind interactions, complicating the Martian space
86 environment. Although many studies in the past several decades have been conducted based on

87 the spacecraft missions such as Phobos-2, Mars Global Surveyor, and Mars Express [e.g.,
88 Yeroshenko et al., 1990; Halekas et al., 2006; Barabash et al., 2007; Fedorov et al., 2006], our
89 knowledge about the magnetic field structure of Mars' magnetosphere is lacking due to limited
90 orbit coverage and inadequate scientific equipment. However, NASA's recent mission on the
91 Mars Atmosphere and Volatile Evolution (MAVEN) spacecraft carried both magnetometer and
92 plasma instruments and provided global coverage of the Martian space environment within $3 R_m$
93 ($R_m = 3390\text{km}$, Mars radius), with an orbit period of about 4.5 hours [Jakosky et al. 2015],
94 enabling us to study the global average magnetic field configuration around Mars.

95 Based on MAVEN observations, Harada et al. [2015] found that the tightly-wrapped field
96 lines and the sunward flow of ionospheric plasma tend to occur in the $-E$ -hemisphere. Inui et al.
97 [2019] pointed out that Martian ions with high speeds form a plume in the $+E$ -hemisphere, while
98 dense and slow-speed ions form an ion trail in the $-E$ -hemisphere. Both simulations and
99 observations show that crustal fields can twist the Martian magnetotail [Luhmann et al., 2015;
100 DiBraccio et al., 2018; Xu et al., 2020]. To lower the possible effects of these fields on
101 magnetospheric field structure, Dubinin et al. [2019, 2021] focused solely on the northern
102 hemisphere to study the field structure of Martian induced magnetosphere; they found that the
103 draping fields wrap the planet in the $+E$ -hemisphere and then propagate toward the $-E$ -
104 hemisphere. By studying the projected distribution of magnetic field in the plane perpendicular
105 to the Sun–Mars line, Chai et al. [2019] argued that a looping magnetic field also rotates around
106 the Martian magnetotail.

107 Although these studies have revealed some characteristics of the magnetic field
108 configuration of the Martian magnetosphere, the 3-D configuration of the field structure and its
109 variations remains unclear. Hence, our goal is (1) to draw the global 3-D magnetic morphology
110 of the Martian magnetosphere based on the magnetic field data collected by MAVEN over a
111 period of 6 years (2014.10–2020.12), and (2) to investigate the possible impacts brought about by
112 the IMF, solar wind pressure, and planet rotation. Overall, such a study would benefit our
113 understanding of solar wind interaction with Mars.

114 **2 Coordinates and Data Set**

115 In this paper, we adopt magnetic field data measured by the Magnetometer (MAG)
116 [Connerney et al., 2015] from 1 October 2014 to 31 December 2020. MAG measures the

117 magnetic field vectors at sample rates 32 Hz and 1 Hz. To minimize the noise and high-
118 frequency fluctuations, we use the data of 1s resolution.

119 Two Cartesian coordinate systems are involved in this study. The first uses Mars-centered
120 Solar Orbital (MSO) coordinates, where the X_{MSO} axis points from the center of Mars to the Sun,
121 the Z_{MSO} axis points to the North Pole of Mars' orbital plane, and the Y_{MSO} axis completes the
122 right-handed system. The second is the Mars Solar Electric coordinates (MSE), where X_{MSE}
123 points antiparallel to the upstream solar wind flow, Y_{MSE} points along the cross-flow magnetic
124 field component of the upstream IMF, and Z_{MSE} points along the direction of the convection
125 electric field in the solar wind. Since the magnetic field configuration of the induced
126 magnetosphere is guided by the IMF orientation, one has to study the 3-D magnetic field
127 structure of the Martian magnetosphere in MSE.

128 To organize magnetic field data in MSE, we select orbits where pristine solar wind can be
129 measured. Similar to procedures adopted by Liu et al. [2021], we first identify orbits with
130 identifiable bow shock crossings according to the jump variation of their magnetic field strength,
131 the ion energy spectrum of the Solar Wind Ion Analyzer (SWIA) [Halekas et al. 2013], and the
132 electron energy spectrum of the Solar Wind Electron Analyzer (SWEA) [Mitchell et al. 2016].
133 Then, for each orbit, we took the average of upstream solar wind 30 minutes before (after) the
134 inbound (outbound) bow shock crossing; the averaged solar wind velocity and IMF are denoted
135 \vec{V}_{sw1} and \vec{B}_1 (\vec{V}_{sw2} and \vec{B}_2), respectively. Because the IMF is usually time-varied, we chose orbits
136 during which the IMF was steady to construct MSE coordinates. This steady IMF is defined
137 when the angle between \vec{B}_1 and \vec{B}_2 is less than 30° . Thus, for a steady IMF, we have

$$138 \quad \vec{X}_{MSE} = -\frac{\vec{V}_{sw1} + \vec{V}_{sw2}}{|\vec{V}_{sw1} + \vec{V}_{sw2}|}, \quad \vec{Y}_{MSE} = \frac{\vec{B}_{\perp 1} + \vec{B}_{\perp 2}}{|\vec{B}_{\perp 1} + \vec{B}_{\perp 2}|}, \quad \text{and} \quad \vec{Z}_{MSE} = \vec{X}_{MSE} \times \vec{Y}_{MSE}. \quad \text{The subscript “}\perp\text{” represents}$$

139 the cross-flow component of the IMF, which can be calculated by subtracting the flow-aligned
140 component, e.g., $\vec{B}_{\perp 1} = \vec{B}_1 - (\vec{B}_1 \cdot \vec{X}_{MSE})\vec{X}_{MSE}$. The direction of \vec{Z}_{MSE} is also the same as that of the
141 solar wind electric field (\mathbf{E}). The Cartesian components of the magnetic field along the X-axis,
142 Y-axis, and Z-axis in MSE are denoted as B_x , B_y , and B_z , respectively.

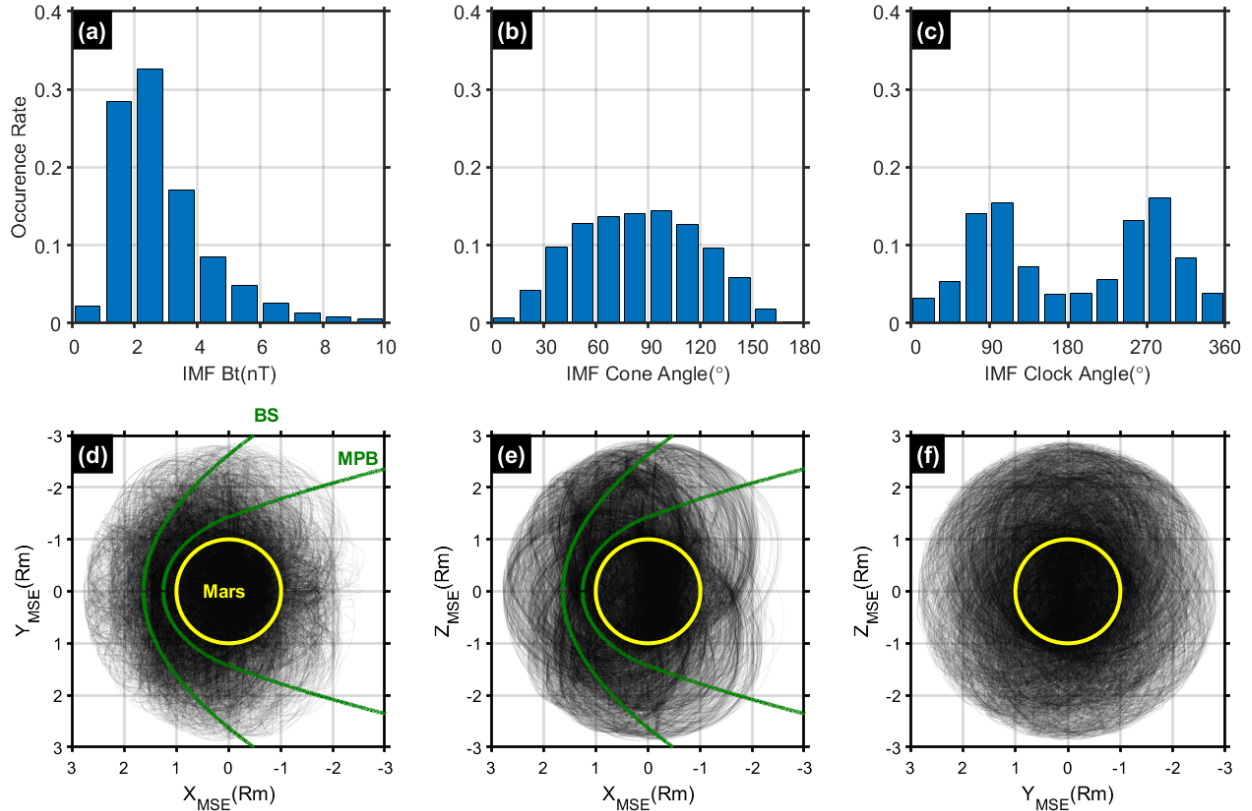
143 We found 4179 orbits in total that satisfy the conditions of a steady IMF; the measured
144 magnetic field vectors in those orbits were transformed into MSE. To exclude the influence of
145 crustal fields, we only kept magnetic field data points satisfying $|B_{obs}| \geq 10|B_{model}|$, where

146 $|B_{obs}|$ is the recorded magnetic field strength and $|B_{model}|$ is the magnetic field strength
 147 predicted by a state-of-the-art crustal fields model [Gao et al., 2021]. These data points constitute
 148 the data set we used in this study. For solar wind parameters corresponding to these orbits, we
 149 averaged those parameters outside the bow shock: for example, the average IMF of one given
 150 orbit is $IMF = \frac{\bar{B}_1 + \bar{B}_2}{2}$.

151 To avoid statistical bias, we checked the IMF distribution of our data set. Figures 1a–1c
 152 shows histograms of the upstream average IMF for each orbit. Here, the IMF strength is mostly
 153 smaller than 5 nT and peaks at ~ 2.5 nT (Figure 1a). The direction of IMF is characterized by its
 154 cone and clock angle. The cone angle—the angle between the IMF and $+X_{MSE}$ —has a unimodal
 155 distribution and peaks at $\sim 90^\circ$ (Figure 1b). The clock angle—the angle between the projected
 156 IMF and $+Z_{MSE}$ in the YZ_{MSE} plane (and which increases rotationally from $+Z_{MSE}$ toward
 157 $+Y_{MSE}$)—exhibits a bimodal distribution with peaks reaching 90° and 270° (Figure 1c). The IMF
 158 distributions in our data set are consistent with typical ones regarding the upstream solar wind
 159 condition at Mars [Liu et al., 2021]. Thus, our data set is statistically significant enough to survey
 160 the average magnetic structure of the Martian induced magnetosphere.

161 As shown in Figures 1d–1f, the spatial region around Mars ($-2 < X_{MSE} < 3 R_m$, $-3 < Y_{MSE} < 3$
 162 R_m , $-3 < Z_{MSE} < 3 R_m$) is adequately accounted for by our data set. In the following sections, we
 163 will study the magnetic field structure within this region (MSE coordinates are used unless
 164 otherwise stated.).

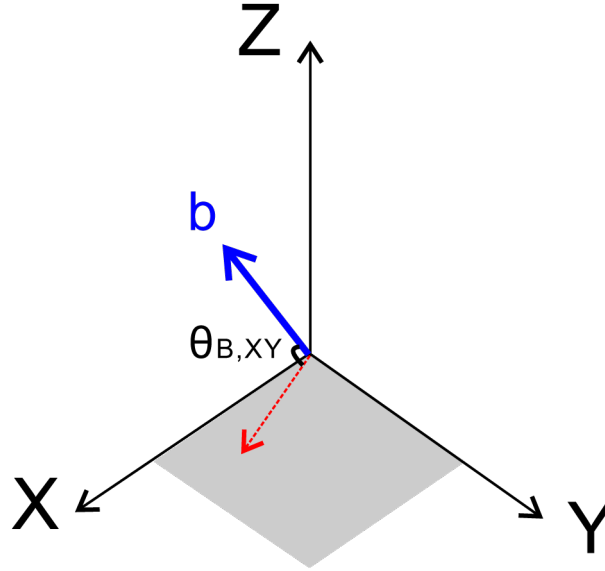
165



166
 167 **Figure 1.** The upper panels show histograms of (a) the IMF strength, (b) the IMF clock angle,
 168 and (c) the IMF cone angle, respectively. The lower panels show orbit coverage of the data set,
 169 projected on the plane of (d) XY_{MSE} , (e) XZ_{MSE} , and (f) YZ_{MSE} , respectively. The yellow circles
 170 represent the body of Mars, while the green curves represent the nominal shape of the bow shock
 171 (BS) and the magnetic pile-up boundary (MPB) [Trotignon et al., 2006].

172 3 Statistical Results

173 To establish and draw the 3-D characteristics of the magnetic field configuration around
 174 Mars, we first check the average two-dimensional distributions of magnetic field vectors in the
 175 slices of the XZ_{MSE} , XY_{MSE} , and YZ_{MSE} planes, respectively, at different locations. Each slice is
 176 partitioned by a bin of 0.2×0.2 Rm, and the field vectors located in the slice are averaged for
 177 each bin. To ensure statistical significance, we ignore bins whose data points are fewer than ten.



178

179 **Figure 2.** The sketched diagram to show the orientation of the unit magnetic field vector. The
 180 blue arrow represents the unit magnetic field vector (\vec{b}), the red arrow denotes the projection of
 181 \vec{b} on XY_{MSE} plane. The $\theta_{B,XY}$ is the angle between \vec{b} and XY_{MSE} plane.

182

183 To study the 3-D field structure, we also need to evaluate how much the average field
 184 vectors deviate from the slices above by calculating the angle between these vectors and the
 185 slices of XZ_{MSE} , XY_{MSE} , YZ_{MSE} planes, respectively:

$$186 \quad \begin{cases} \theta_{B,XZ} = a \sin(b_y) \\ \theta_{B,XY} = a \sin(b_z) \\ \theta_{B,YZ} = a \sin(b_x) \end{cases} \quad (1)$$

187 where b_x , b_y , b_z represent the x, y, z component of the average unit magnetic field vector
 188 respectively in the bin. Taking $\theta_{B,XY}$ as an example (see Figure 2), the $\theta_{B,XY}=90^\circ(-90^\circ)$
 189 represents that the field lines are pointing along $+Z_{MSE}$ ($-Z_{MSE}$), while $\theta_{B,XY}=0^\circ$ represents the
 190 field lines are parallel to XY_{MSE} plane. Furthermore, a larger $\theta_{B,XY}$ indicates is the field lines are
 191 more perpendicular to the XY_{MSE} plane.

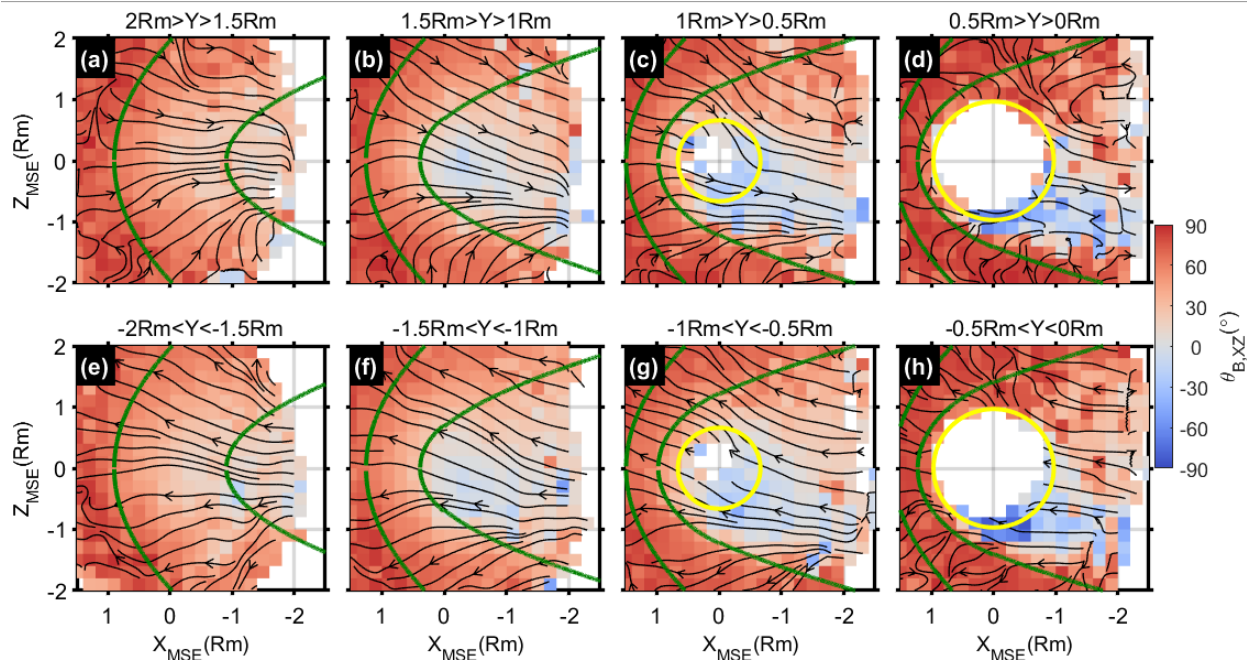
192 **3.1 Magnetic Field Structure in XZ Plane**

193 We first check the distribution of the magnetic field in different slices of XZ_{MSE} planes, with
 194 each slice having a thickness of $0.5 R_m$ within $-2R_m < Y_{MSE} < 2R_m$. Based on the average
 195 distribution of the B_x , B_y , and B_z components in the bin of each slice, we can plot the average
 196 projected magnetic field lines (MFLs) in the XZ_{MSE} plane, while calculating the $\theta_{B,XZ}$ according
 197 to Eq. (1).

198 In Figure 3, the upper panels show field distributions for slices in the $+Y_{MSE}$ -hemisphere
 199 (Figures 3a–3d), while the lower panels do so for slices in the $-Y_{MSE}$ -hemisphere (Figures 3e–
 200 3h). As we can see, the MFLs are directed tailward (sunward) in the $+Y_{MSE}$ ($-Y_{MSE}$) –
 201 hemisphere, which means the IMF, pointing basically towards the $+Y_{MSE}$ direction, begins
 202 draping near the planet. Meanwhile, we notice that, from both flanks along Y_{MSE} to the central
 203 meridian, the draping MFLs outside the magnetic pile-up boundary tilt towards the nightside
 204 magnetic equatorial plane ($\sim Z_{MSE} = 0$); thus, the MFLs looks like they are “sinking” into the
 205 Martian wake. This pattern is reminiscent of the “sinking fields” observed in the Venusian
 206 magnetotail [Rong et al., 2014]. We also notice that the “sinking fields” from $+Z_{MSE}$ –hemisphere
 207 can extend down to $\sim Z_{MSE} = -1 R_m$; thus, “sinking fields” are more significant in the $+Z_{MSE}$ –
 208 hemisphere than in the $-Z_{MSE}$ –hemisphere, which is consistent with the hemispheric asymmetry
 209 of “sinking fields” reported by Rong et al. [2014] in the Venusian tail. Recent studies by Dubinin
 210 et al. [2019, 2021] have likewise reported the E-asymmetry of draping field structure in Martian
 211 tail.

212 Meanwhile, outside both flanks ($|Y_{MSE}| > 1.5 R_m$; see Figures 3a and 3e), the “sinking” field
 213 lines from both $\pm E$ -hemispheres are basically symmetrical respective to the plane of $Z_{MSE} = 0$,
 214 indicating that the E-asymmetry is weaker there.

215



216

217 **Figure 3.** Average distributions of $\theta_{B,XZ}$ in the slices of the XZ_{MSE} plane within different ranges
 218 of the Y_{MSE} coordinate. Overplotted black lines with arrows denote the average MFLs. MFLs
 219 with red- (blue)-colored regions mean MFLs have a positive (negative) B_y component. In each
 220 panel or slice, the yellow circle represents the mean cut of Mars' body while the two green
 221 curves represent the mean cut of the nominal BS, MPB shape. Taking panel c as an example, the
 222 two green curves and the yellow circle are cuts of the BS, MPB shape and Mars' body,
 223 respectively, at $Y_{MSE}=0.75$ Rm.

224

225 Additionally, when approaching the central meridian from both flanks, the polarity of B_y
 226 component in some parts of the $-E$ -hemisphere becomes negative (see negative $\theta_{B,XZ}$ in Figure
 227 3); thus, corresponding MFLs seem stretched (Figures 3b–3c and Figures 3f–3g) and even
 228 “pinched” nearer the central meridian (Figures 3d–3h). Both “sinking” and “pinched” effects
 229 show that MFLs in the $-E$ -hemisphere are tightly wrapped around the planet.

230 3.2 Magnetic Field Structure in XY Plane

231 Using the same procedures in subsection 3.1, we examine the magnetic field structure in
 232 slices of the XY_{MSE} plane.

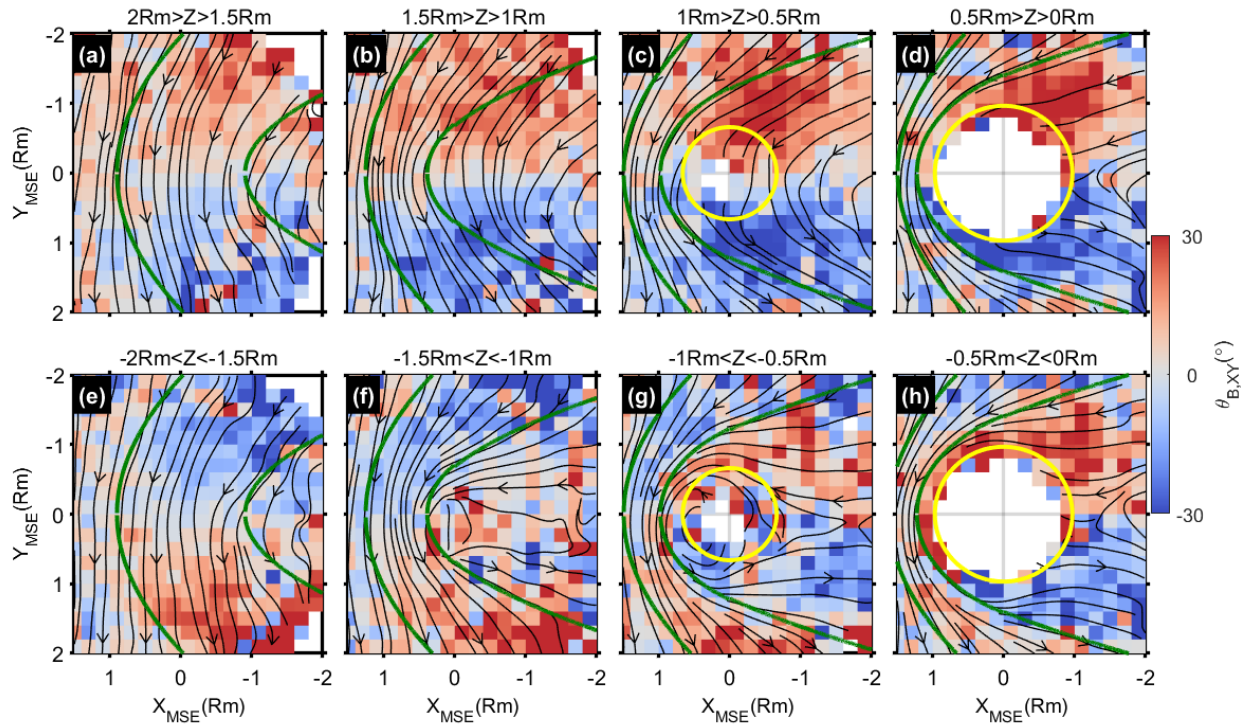
233 Figure 4 shows distributions of $\theta_{B,XY}$ and the average MFLs in slices of the XY_{MSE} plane
 234 with a thickness of $0.5 R_m$ from $Z_{MSE} = 2R_m$ to $Z_{MSE} = -2R_m$.

235 Clearly, each panel of Figure 4 shows an IMF that basically points towards $+Y_{MSE}$ in the
 236 upstream and bends upon approaching the planet. The bent MFLs are draped around the planet,
 237 which results in a positive B_x in the $-Y_{MSE}$ -hemisphere and a negative B_x in the $+Y_{MSE}$ -
 238 hemisphere. From the flanks of both $\pm E$ -hemispheres to the equator region ($Z_{MSE} = 0$), the
 239 draped MFLs are more tightly wrapped around the planet on the dayside and the field lines more
 240 stretched in the down tail.

241 Interestingly, the field lines in the wake of the $-E$ -hemisphere are highly stretched and are
 242 even “pinched” towards the central meridian or plasma sheet (Figures 4f - 4h). The “pinched”
 243 field lines in the $-E$ -hemisphere correspond to the negative B_y component, as noted in Figure 3.

244 It is important to note from Figure 4 that $\theta_{B,XY}$ in the $+E$ -hemisphere is positive (negative)
 245 when $Y_{MSE} < 0$ ($Y_{MSE} > 0$), a feature that extends even to the $-E$ -hemisphere (Figures 4g - 4h). In
 246 contrast, the opposite distribution pattern of $\theta_{B,XY}$ only occurs near the flank of $-E$ -hemisphere
 247 (Figures 4e - 4f). The distribution of $\theta_{B,XY}$ demonstrates that the draped MFLs with $Z_{MSE} > -1$
 248 R_m “sinks” towards the $-E$ -direction, while the draped MFLs with $Z_{MSE} < -1 R_m$ “sinks” towards
 249 the $+E$ -direction. The E -asymmetry of these “sinking” field lines, as demonstrated by Figure 4, is
 250 consistent with our findings in Figure 3.

251



252

253 **Figure 4.** Average distributions of $\theta_{B,XY}$ in slices of the XY_{MSE} plane within different ranges of
 254 Z_{MSE} coordinates. Overplotted black lines with arrows denote the average MFLs. The format is
 255 the same as that of Figure 3.

256

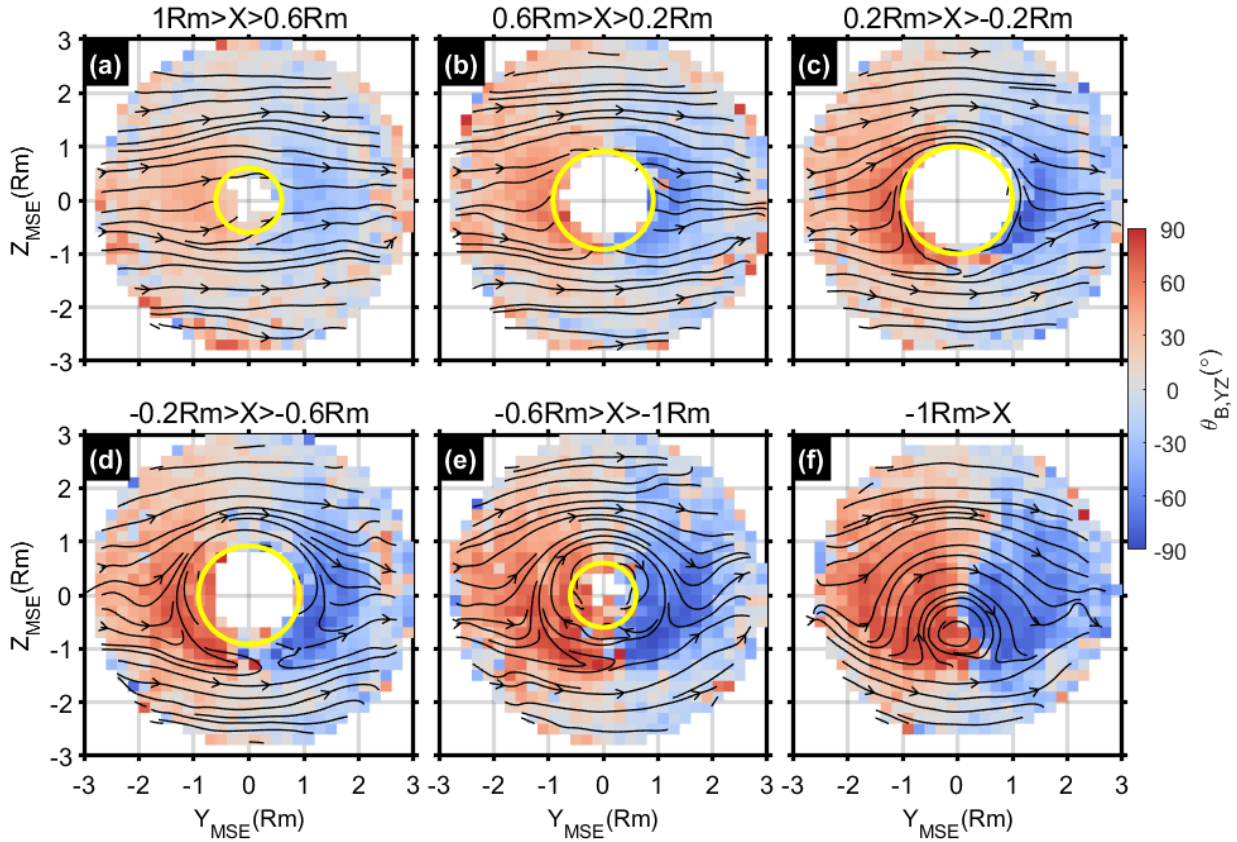
257 3.3 Magnetic Field Structure in YZ Plane

258 Now we examine the magnetic field structure in slices of the YZ_{MSE} plane. Figure 5 shows
 259 distributions of $\theta_{B,YZ}$ and the average MFLs in slices of the YZ_{MSE} plane, with thickness $0.4 R_m$,
 260 from dayside to nightside. Again, distributions of $\theta_{B,YZ}$ indicate that the magnetic field has a
 261 positive B_x component in the $-Y_{MSE}$ -hemisphere and a negative B_x component in the $+Y_{MSE}$ -
 262 hemisphere, which suggests that MFLs are bent with respect to $Y_{MSE}=0$ and are draped around
 263 the planet.

264 In the YZ_{MSE} plane, MFLs on the dayside point basically along $+Y_{MSE}$ direction (Figures
 265 5a – 5b); nonetheless, as X_{MSE} moves downstream, the pattern of the MSLs becomes bulge-like
 266 when $Z_{MSE} > -1 R_m$ and more concave-like when $Z_{MSE} < -1 R_m$ (Figures 5c–5f). When we

267 consider the reversed polarity of the B_x component with respect to the plane $Y_{MSE}=0$, these
 268 bulge-like or concave-like patterns correspond to “sinking field” projections on the YZ_{MSE} plane.

269 It is interesting to note that the dominance of bulge-like MFLs around the planet ($Z_{MSE} > -1$
 270 R_m) results in the appearance of the “loop field” as presented by Chai et al. [2019].



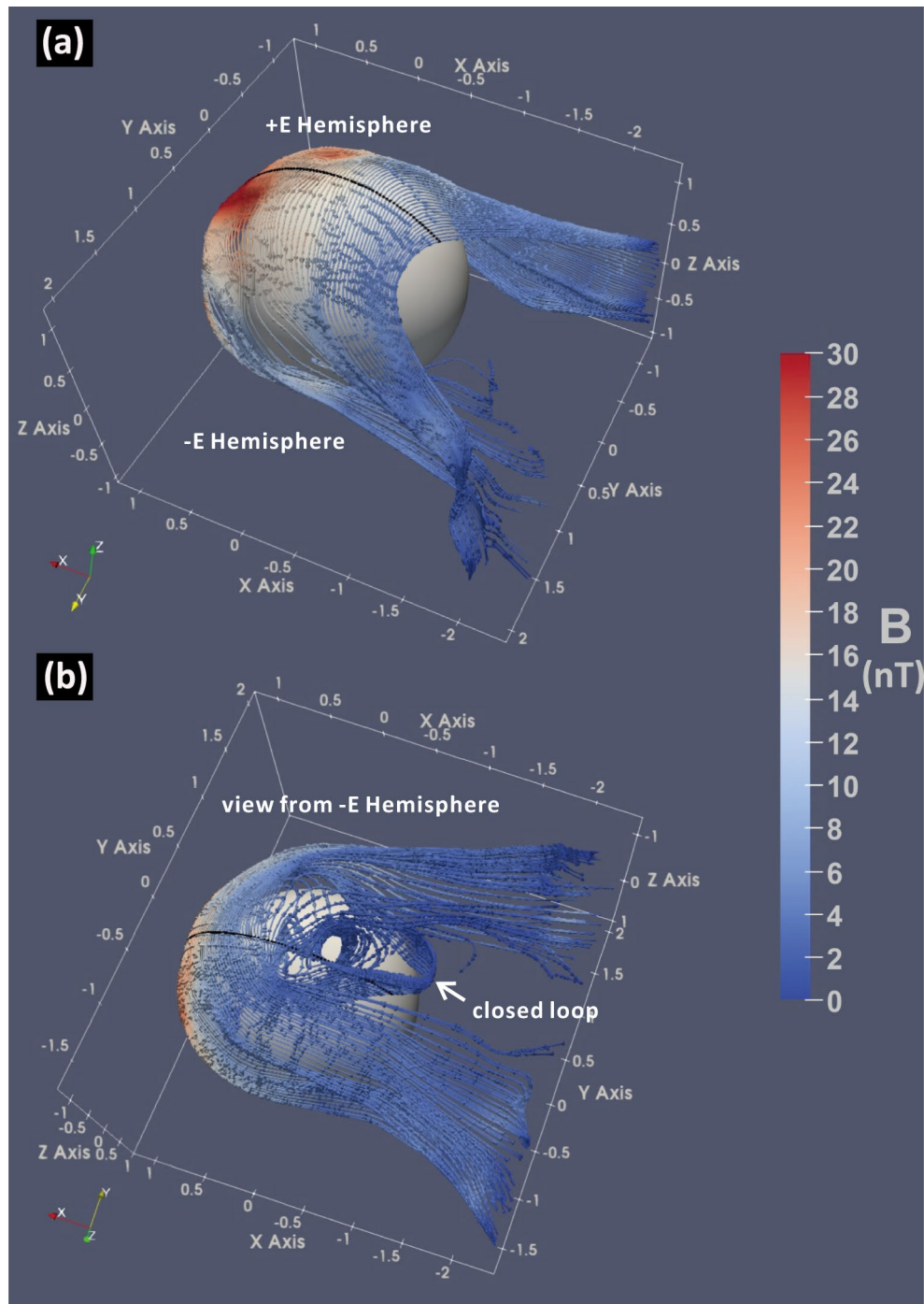
271
 272 **Figure 5.** Average distributions of $\theta_{B,YZ}$ in slices of the YZ_{MSE} plane within different ranges of
 273 the X_{MSE} coordinate. Overplotted black lines with arrows denote average MFLs. The format is
 274 the same as that of Figure 3.

275

276 3.4 Visualization of 3-D MFLs

277 In the above subsections, we studied the projection of the magnetic field structure on
 278 different planes. Here, we draw the global 3-D magnetic field configuration directly by
 279 partitioning the spatial volume $X_{MSE}(-3 \sim 3R_M) * Y_{MSE}(-3 \sim 3R_M) * Z_{MSE}(-3 \sim 3R_M)$ by a bin of $0.2R_m$

280 $\times 0.2R_m \times 0.2R_m$ and averaging the data points in each bin. Using these averaged data points,
 281 we plot the 3-D configuration of MFLs around Mars in Figure 6.



282

283 **Figure 6.** Average 3-D magnetic field lines in (a) the +E-hemisphere ($Z_{MSE} > 0$) and (b) the E-
 284 hemisphere ($Z_{MSE} < 0$). MFLs are colored according to field strength. The black dots in the XZ_{MSE}
 285 plane are the starting points for tracing the average MFLs, which are equally spaced within the
 286 solar zenith angle range of $0^\circ \sim 135^\circ$ with constant altitude of $0.2 R_m$.

287 As shown in Figure 6a, the configuration of MFLs in the +E-hemisphere is largely
 288 consistent with the classical draping pattern: that is, the MFLs flare with respect to the plane of
 289 $Y_{MSE}=0$, and these flaring field lines, after slipping over the terminator, tilt towards the magnetic
 290 equatorial plane as “sinking” fields. Nonetheless, the draped MFLs near the magnetic equatorial
 291 plane do not flare significantly but are “pinched” towards the central meridian in the wake. In
 292 contrast to Figure 6a, the draped MFLs in the E-hemisphere are generally “pinched” towards the
 293 central meridian in the wake (Figure 6b). We notice, in particular, that a closed magnetic loop
 294 could form over the pole of -E-hemisphere, which is consistent with the picture shown in Figure
 295 4g. This magnetic loop was also noticed in previous studies [Dubinin et al., 2019; 2021].

296 **4. Average Structure of the Magnetotail Current Sheet**

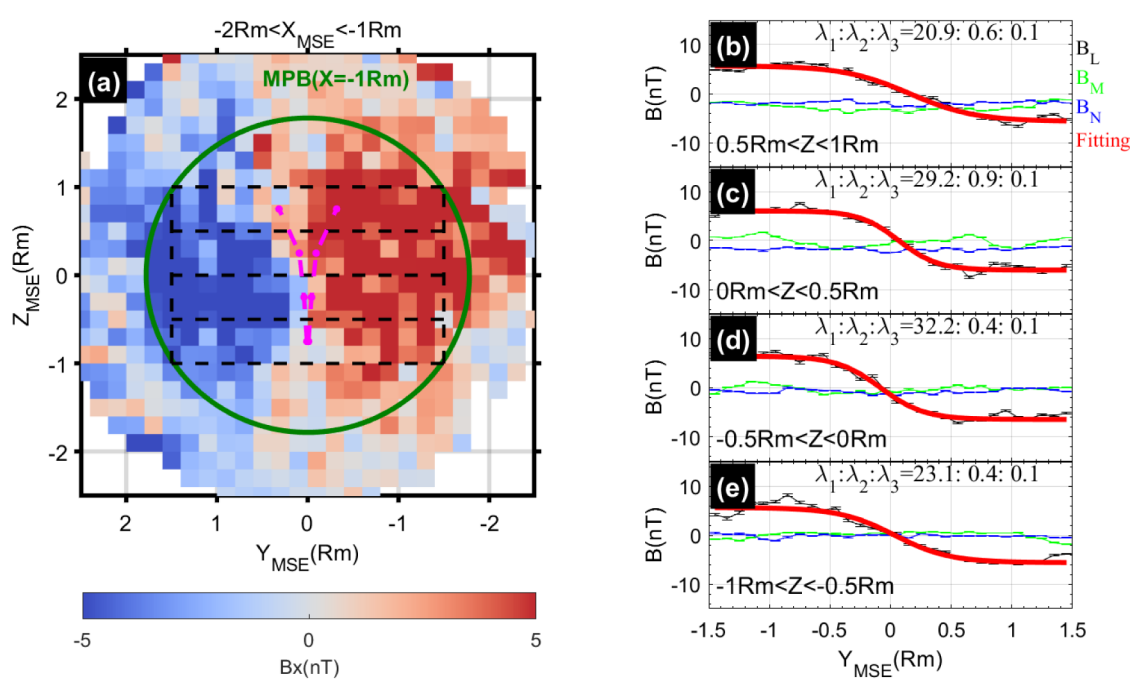
297 As mentioned above, there is an evident E-asymmetry of the draped field lines in the
 298 Martian wake, which may imply a similar E-asymmetry in the structure of the induced
 299 magnetotail current sheet. In this section, we attempt to quantitatively diagnose the averaged
 300 properties of Martian current sheet, which will enable us to interpret the plasma dynamics of
 301 current sheet.

302 To consider the orbit coverage of MAVEN while avoiding the influence of the
 303 magnetosheath (see Figure 1), we confine the studied tail region to $-1R_m < X_{MSE} < -2 R_m$ and
 304 $|Y_{MSE}| < 1.5R_m$, and show the distribution of B_x component in Figure 7a. It is clear from Figure
 305 7a that a tail current sheet separating two lobes with an opposite polarity of the B_x component is
 306 located at $Y_{MSE} \sim 0$. To survey the possible variations of the current sheet structure along the
 307 Z_{MSE} -axis, we study four regions of the magnetic field structure within Z_{MSE} -axis ranges: that is,
 308 $0.5 R_m < Z_{MSE} < 1R_m$, $0 < Z_{MSE} < 0.5R_m$, $-0.5 R_m < Z_{MSE} < 0$, and $-1R_m < Z_{MSE} < -0.5 R_m$ (see black
 309 dashed regions in Figure 7a). We project the location of MPB at $X_{MSE} = -1R_m$ onto Figure 7a
 310 (see the green circle). Since the radius of MPB increases as it moves tailward, $X_{MSE} = -1R_m$ is the
 311 lowest limit of MPB in our studied region. It is apparent that these four regions are inside the
 312 MPB.

313 To estimate the magnetic field structure over the current sheet in each region, we have to
 314 check the profiles of the magnetic field over the current sheet. Because the B_x component and
 315 the B_z component are correlated in Martian magnetotail (see Figure 3), minimum variance

316 analysis (MVA) of the magnetic field in each region [Sonnerup & Scheible,1998] can help
 317 remove such correlations. MVA yields three eigen values ($\lambda_1 \geq \lambda_2 \geq \lambda_3 > 0$) and their corresponding
 318 eigenvectors $\{\vec{L}, \vec{M}, \vec{N}\}$. The three eigenvectors represent the directions of maximum,
 319 intermediate, and minimum variance of the magnetic field. They are orthogonal and constitute a
 320 local coordinate of the current sheet ($\vec{L} = \vec{M} \times \vec{N}$). \vec{L} points along the magnetic field direction in
 321 the lobe, \vec{M} is basically along \vec{E}_{SW} and tangential to the current sheet plane, and \vec{N} is the
 322 normal of current sheet and points basically along the Y_{MSE} -axis. The components of the average
 323 magnetic field along \vec{L} , \vec{M} , and \vec{N} are labelled B_L , B_M , and B_N .

324 The average profiles of B_L (black lines), B_M (green lines), and B_N (blue lines) against Y_{MSE}
 325 for each region are shown in Figures 7b-7e. For all the regions, the B_M and B_N components are
 326 basically constant, while B_L varies significantly over the current sheet ($Y_{MSE} \sim 0$ plane), which
 327 demonstrates that the field structure of the Martian tail current sheet is one-dimensional (1-D).
 328 Because the yielded \vec{L} for each region is well distinguished from \vec{M} and \vec{N} , as demonstrated
 329 by $\lambda_1 \gg \lambda_2, \lambda_3$, and the normal direction \vec{N} is basically aligned with the Y_{MSE} axis (not shown
 330 here), we could fit the profiles of B_L to a typical 1-D Harris sheet model: e.g.,
 331 $B_L = B_0 \tanh\left(\frac{Y_{MSE} - y_0}{L}\right)$ [Harris, 1962], where B_0 is the lobe field strength, L is the typical scale
 332 of the sheet, and y_0 is the normal shift of the sheet center. Coefficients of the adjusted R-square
 333 (>0.9) indicate that the fitting results are satisfactory (see Table 1).



334
 335 **Figure 7.** The left panel shows the distribution of B_x in the Martian magnetotail ($-2R_m < X_{MSE} < -1R_m$). The green cycle marks the nominal MPB shape when $X = -1R_m$. The tail region is
 336 partitioned into four regions (rectangles marked by dashed lines, each with a width of $3R_m$ and a
 337 height of $0.5R_m$ from $Z_{MSE} = -1R_m$ to $Z_{MSE} = +1R_m$). The magenta dashed lines outline the
 338 thickness of the current sheet according to the curvature radius of the MFLs. The right panel
 339 shows the average profiles of B_L (black lines), B_M (green lines), and B_N (blue lines) against Y_{MSE}
 340 in each region. The lengths of the error bars are $2 \times 1.96 \frac{\sigma}{\sqrt{n}}$, representing a 95% confidence
 341 interval, where $\frac{\sigma}{\sqrt{n}}$ is the standard error of the mean. The red dashed lines denote the fit curves
 342 of the Harris sheet model. The ratio of the three eigenvalues derived from MVA are labelled.
 343
 344

345 Based on the fitted parameters, the cross-tail current density at sheet center, which flows
 346 basically towards \mathbf{E} , can be estimated as $J = \frac{B_0}{\mu_0 L}$, and the minimum curvature radius of MFLs
 347 reached at the sheet center can be estimated as $R_{c,\min} = \frac{\langle B_N \rangle L}{B_0}$, if B_M is omitted, where
 348 $\langle B_N \rangle$ is the average B_N component over the current sheet. $R_{c,\min}$ can be regarded to have half
 349 the thickness of the current sheet [e.g., Rong et al., 2014; Shen et al., 2007]. The resulting
 350 tailward Ampere force at the sheet center can be roughly estimated as $J \times B \sim J \langle B_N \rangle$. Fitted
 351 parameters are listed in Table 1.

352 **Table 1.** Estimated Parameters of the Magnetotail Current Sheet in Different Regions

Region	B_0 (nT)	L (Rm)	R^2	$\langle B_N \rangle$ (nT)	R_{c_min} (Rm)	J (nA/m ²)	$\vec{J} \times \vec{B}$ (nT*nA/m ²)
0.5Rm < Z < 1 Rm	5.67	0.54	0.97	3.35	0.32	2.48	-8.31
0 < Z < 0.5Rm	6.05	0.32	0.98	1.78	0.09	4.47	-7.96
-0.5Rm < Z < 0	6.42	0.36	0.98	0.75	0.04	4.23	-3.17
-1Rm < Z < -0.5Rm	5.62	0.45	0.95	-0.12	0.009	2.93	0.35

353 ^a R^2 is the coefficient of the adjusted R square, which indicates fitting goodness (closer to one
354 means a better fit).

355 ^b $\langle B_N \rangle$ is the averaged value of B_N over the range $-1.5R_m < Y_{MSE} < 1.5R_m$.

356 ^c R_{c_min} is the estimated magnetic field curvature radius at the center of current sheet.

357 ^dJ is the estimated current density at the center of current sheet.

358 ^e This is the estimated force of $J \times B$ at the center of current sheet. The +/- sign means the
359 direction of $J \times B$ is sunward/tailward.

360

361 From Table 1, the Martian magnetotail has an evident E-asymmetry: the current sheet in the
362 +E-hemisphere has a larger B_N component, is thicker, and has a stronger tailward Ampere force,
363 but in the -E-hemisphere the sheet has a smaller B_N component, is thinner, and has a weaker
364 Ampere force. The polarities of B_N and $\vec{J} \times \vec{B}$ are even reversed in the region of $-1R_m < Z < -$
365 $0.5R_m$. The E-asymmetry of $\vec{J} \times \vec{B}$ demonstrates that ampere force (which plays out as magnetic
366 tension force) can accelerate plasma sheet ions moving tailward, so that tailward velocity is
367 greater near the flank of +E-hemisphere. Considering the number density of ionospheric plasma
368 ions $\sim 1\text{cm}^{-3}$ ($\sim 5\text{cm}^{-3}$) in +E (-E)-hemisphere [Inui et al., 2019], and the average of $\vec{J} \times \vec{B}$ is -
369 $8.31\text{ nT} \cdot \text{nA/m}^2$ ($-3.17\text{ nT} \cdot \text{nA/m}^2$) in +E (-E) hemisphere, these ions could be accelerated to
370 $\sim 180\text{eV}$ ($\sim 15\text{eV}$) within a distance of $1R_m$ in the +E (-E) hemisphere by $\vec{J} \times \vec{B}$ (the accelerated
371 energy equals the product of $\vec{J} \times \vec{B}$ and distance). Thus, the ions in the current sheet can be
372 accelerated to a faster speed in the +E-hemisphere than that in the -E-hemisphere, which is
373 consistent with previous observations [Dubinin et al., 2019; Inui et al., 2019]. Furthermore, the
374 sunward $\vec{J} \times \vec{B}$ near the flank of the -E-hemisphere might explain, to some extent, sunward ions
375 that tend to occur in the -E-hemisphere [Harada et al., 2015]. Further studies are necessary to
376 address this issue.

377 In contrast to E-asymmetry, the lobe field B_0 is basically constant (5~6 nT) in the whole
378 magnetotail. Current density at the current sheet center is relatively higher near the magnetic
379 equator ($-0.5 R_M < Z_{MSE} < 0.5 R_M$) than the current density near both flanks ($0.5 R_M < |Z_{MSE}| < 1$

380 R_M), and the distribution pattern is consistent with a previous study (see Figure 3b of Ramstad et
 381 al. [2020]).

382

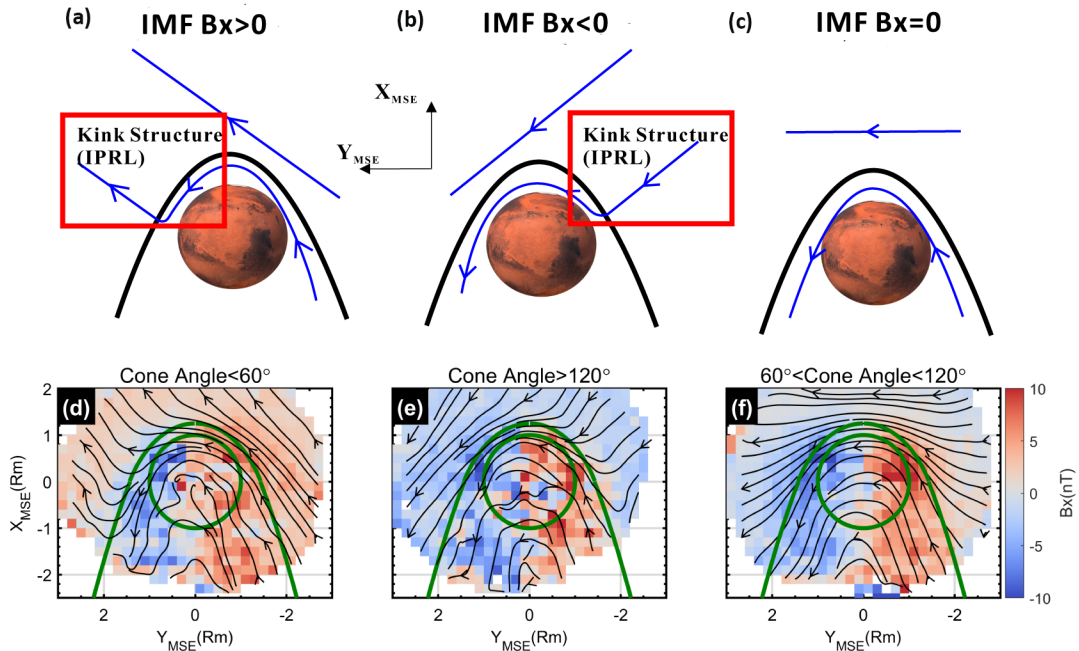
383 **5. Influence of Solar Wind Conditions and Crustal Fields**

384 **5.1 Influence of IMF B_x**

385 Previous studies on the induced magnetosphere of Venus have demonstrated that the
 386 polarity of IMF B_x could modulate the draping of IMF around the planet [e.g., McComas et al.,
 387 1986; Rong et al., 2016; Delva et al., 2017]. As sketched in Figures 8a–8b, under the presence of
 388 significant upstream IMF B_x component, a kink-like field structure named inverse polarity
 389 reversal layer (IPRL) (which a spacecraft would record when crossing it) [Romanelli et al., 2015]
 390 would appear at the boundary of an induced magnetosphere. This IPRL would disappear when
 391 IMF $B_x \sim 0$ (Figure 8c). However, IPRL on Mars has been seldom reported. Here, we use our
 392 data set to check the effect of IMF B_x on the induced magnetosphere of Mars.

393 Our data set, which we confined to $|Z_{MSE}| < 1.5R_M$, is divided into three subdatasets or
 394 conditions: (1) IMF $B_x < 0$ (cone angle $< 60^\circ$), (2) IMF $B_x > 0$ (cone angle $> 120^\circ$), and (3) IMF
 395 $B_x \sim 0$ ($60^\circ < \text{cone angle} < 120^\circ$). We applied the procedure from Section 3 and plotted average
 396 MFLs for each subdatasets respectively in Figures 8d – 8f. From the patterns of the average
 397 MFLs, one can clearly see that the IPRL is located at the magnetospheric boundary of $+Y_{MSE}$ -
 398 hemisphere ($+Y_{MSE}$ -hemisphere) under IMF $+B_x$ ($-B_x$). In contrast, IPRL disappears when IMF
 399 B_x is negligible (Figure 7f). Simulation demonstrates that the density of oxygen ion is enhanced
 400 in IPRL [Jarvinen et al., 2010]. Given the kink-like structure of IPRL, we suggest that IPRL
 401 would induce sunward $\vec{J} \times \vec{B}$ or magnetic tension, which might counterbalance the tailward
 402 plasma flow to some extent and cause ion enhancement.

403 Previous studies suggest that IMF B_x could also shift the Venusian magnetotail current
 404 sheet and bring hemispheric asymmetry to the lobe magnetic flux [McComas et al., 1986], but
 405 this effect is questioned by Rong et al. [2016]. Based on a limited data point of MGS, Romanelli
 406 et al. [2015] argued that IMF B_x could shift the Martian magnetotail current sheet. The effect of
 407 IMF B_x on the Martian magnetotail lies will be addressed exclusively in another paper.



408

409 **Figure 8.** Draping configuration of magnetic field lines under (a) IMF +Bx, (b) IMF -Bx, and (c)
 410 IMF Bx~0. The distribution of Bx and MFLs under (d) IMF +Bx (cone angle<60°), (e) IMF -Bx
 411 (cone angle>120°), and (f) IMF Bx~0 (60°<cone angle<120°), respectively.

412

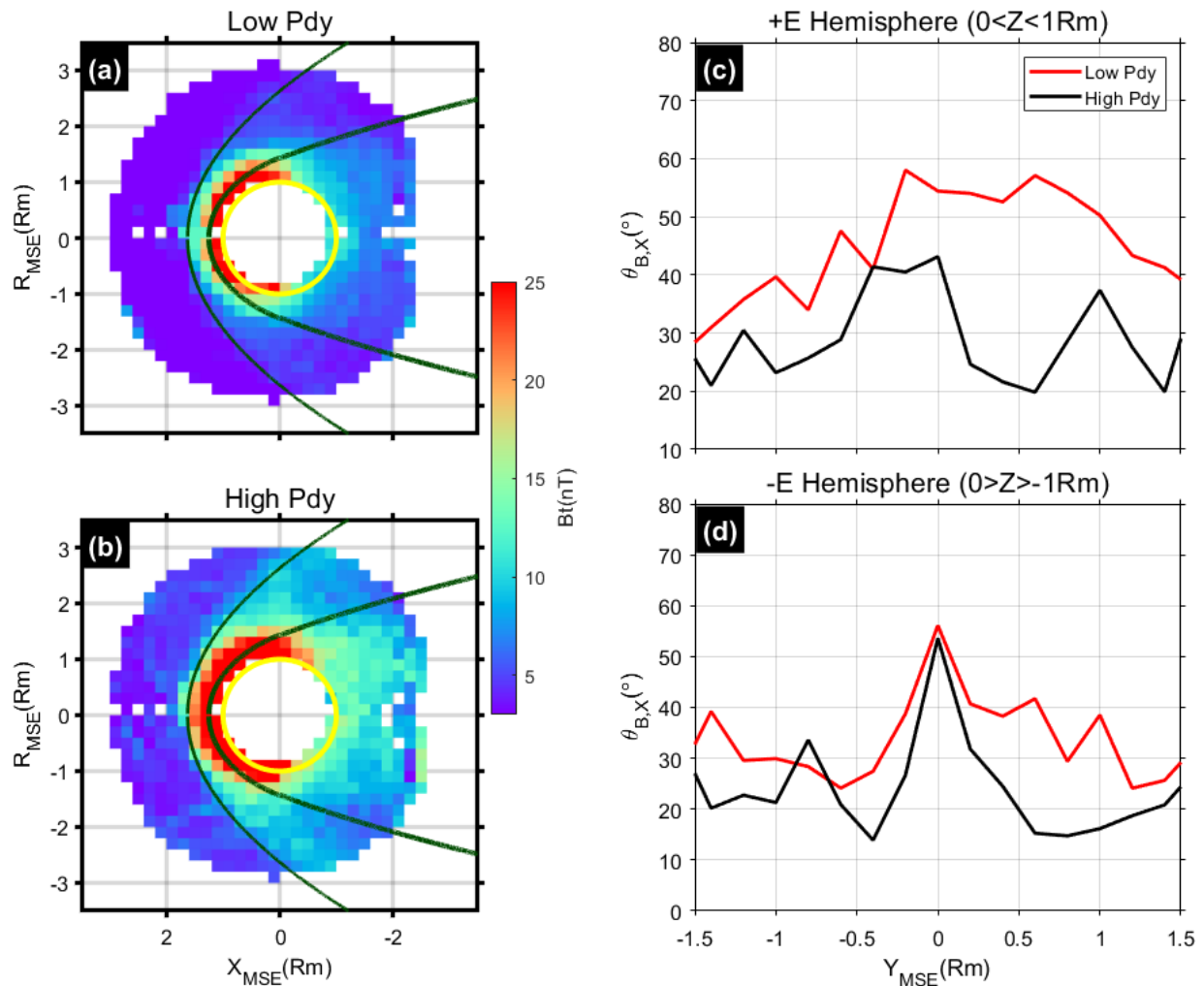
413 5.2 Influence of Solar Wind Dynamic Pressure

414 Solar wind dynamic pressure (P_{dy}) is believed to significantly impact the magnetic
 415 structure of an induced magnetosphere and ion escape [e.g. Ramstad et al., 2015; Dubinin et al.,
 416 2017; Nilsson et al., 2010, 2011; Zhang et al., 1994; Zhang et al., 2021]. Based on our dataset,
 417 we quantitatively evaluate how P_{dy} affects the magnetic field structure around Mars. To facilitate
 418 this, our dataset is dichotomized according to the median value of P_{dy} , i.e. 0.54 nPa. Data points
 419 with a P_{dy} higher than the median constitute a high P_{dy} subdataset, while those lower constitute
 420 a low P_{dy} subdataset. Comparing field distributions and configurations of these two subdatasets
 421 could highlight the effects of P_{dy} .

422 Distributions of magnetic field strength for the two subdatasets above demonstrate that
 423 magnetic fields around the planet, from the magnetosheath to the magnetic barrier as well as the
 424 whole magnetotail, are usually stronger during higher P_{dy} (Figures 9a–9b). This is plausible
 425 because draped MFLs are expected to be more compressed during higher P_{dy} .

426 In addition to the field strength, P_{dy} may also affect the flaring of the draped MFLs [Zhang
 427 et al., 1994]. Here, the flaring angle of MFLs, defined as $\theta_{B,X} = a \cos(\vec{b} \cdot \vec{x})$, shows how much
 428 the magnetic field deviates from the x-axis. By surveying the response of $\theta_{B,X}$ to P_{dy} , we find
 429 that the magnetic field has a relatively smaller $\theta_{B,X}$ during higher P_{dy} than lower ones in the +E-
 430 hemisphere (Figure 9c). Thus, the draped MFLs in the +E-hemisphere generally stretch more or
 431 flare less during higher P_{dy} . The response of $\theta_{B,X}$ to P_{dy} in the -E-hemisphere, though less
 432 significant, is somewhat similar to that in the +E-hemisphere (Figure 9d). The reason seems
 433 obvious: MFLs with less flaring in the -E-hemisphere (see Figure 3) should be less sensitive to
 434 the impact of P_{dy} .

435



436

437 **Figure 9.** Response of the Martian induced magnetic field to dynamic pressure of solar wind.
 438 The left column shows the distributions of magnetic field strength during (a) lower Pdy and (b)
 439 higher Pdy. The Y coordinate is defined as $R_{MSE} = \text{sign}(Z_{MSE}) * \sqrt{Y_{MSE}^2 + Z_{MSE}^2}$. The right
 440 column shows variations of the flaring angle $\theta_{B,XZ}$ against Y_{MSE} in (c) the +E-hemisphere and
 441 (d) the –E-hemisphere. Variation during during lower/higher Pdy is colored red/black.

442

443 5.3 Influence of Crustal Field Rotation

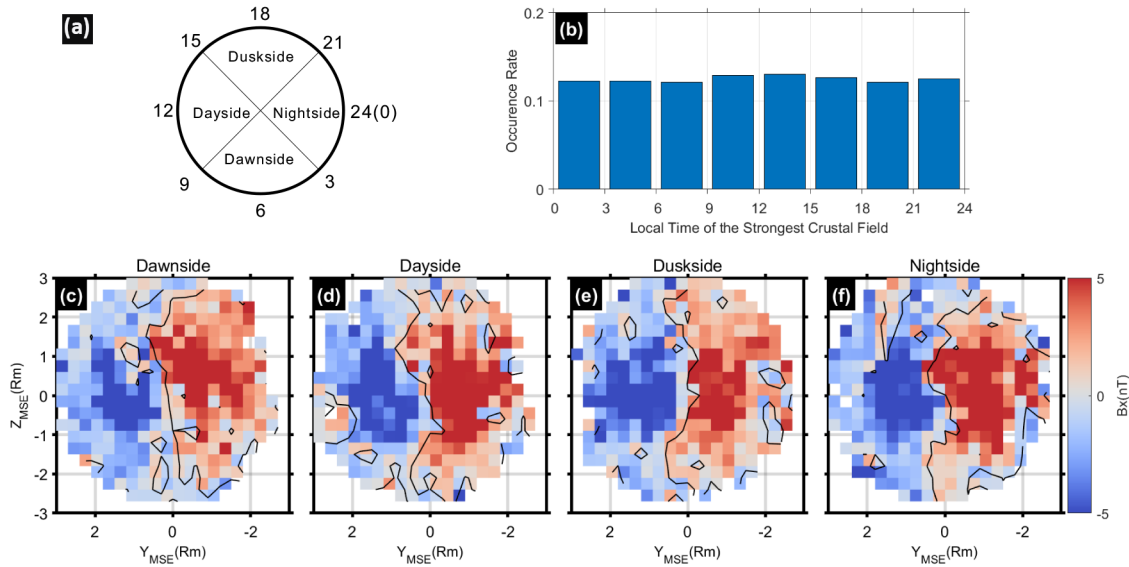
444 Previous studies suggested that the Martian magnetotail current sheet could be twisted by
 445 open field lines owing to the reconnection between the IMF and crustal fields [Luhmann et al.,
 446 2015; DiBraccio et al., 2018; Xu et al., 2020]; crustal fields may also influence the escape of
 447 Martian ions [e.g. Fang et al., 2010; Ramstad et al., 2016; Nilsson et al., 2011; Dubinin et al.,
 448 2020; Zhang et al., 2021]. Although the data points in our dataset are nearly unaffected by the
 449 crustal fields ($B_{model} < 0.1B_{obs}$), one cannot rule out their possible effects on the field structure of
 450 Martian magnetotail. Given Mars' rotation, the crustal field should diurnally modulate the tail
 451 field structure. Thus, in order to survey the effect of the crustal field, we check the response of
 452 the magnetic field distribution of Martian tail ($-1R_m > X > -2R_m$) to the planet's rotation.

453 To simplify the study, the dataset is divided into four subdatasets according to the local time
 454 (LT) when the strongest crustal fields are located at geo-longitude $\sim 178^\circ$ on the Martian surface
 455 (Figure 10a): (1) dawnside ($3 < LT < 9$), (2) dayside ($9 < LT < 15$), (3) duskside ($15 < LT < 21$), and (4)
 456 nightside ($21 < LT & LT < 3$). Because the IMF Bx component may shift the tail current sheet and
 457 bring about lobe asymmetry of magnetic flux [McComas et al., 1986], we only retain—to
 458 highlight possible effects brought about by planetary rotation—the data points with negligible
 459 IMF Bx ($60^\circ < \text{cone angle} < 120^\circ$). Each of these data points has a corresponding LT of the
 460 strongest crustal fields, and the nearly uniform distribution of data points against these LTs rules
 461 out significant statistical bias among the four subdatasets (Figure 10b).

462 For these four subdatasets, we show distributions of Bx in the Martian tail when the
 463 strongest crustal field is located on the dawnside, the dayside, the duskside, and the nightside,
 464 respectively (Figures 10c–10f). Clearly, the distribution patterns of the subdatasets are similar;

465 all tail current sheets are roughly located at $Y_{MSE} \sim 0$. Thus, the rotation of crustal fields cannot
 466 significantly affect or modulate the configuration of the tail current sheet.

467



468

469 **Figure 10.** Effect of Martian rotation on tail field distribution. (a) Diagram of the four sectors
 470 chosen according to the local time of the strongest crustal field. (b) Distribution of data points
 471 against the local time of the strongest crustal field. The distribution of B_x in the YZ plane ($-$
 472 $2 < X < -1$ Rm) when the strongest crustal field is on (c) the dawn side, (d) the day side, (e) the
 473 dusk side, and (f) the night side. Contours of $B_x = 0$ are shown as black lines.

474

475 6 Discussion and Conclusion

476 In this study, which is based on a statistical survey of magnetometer measurements made by
 477 MAVEN from approximately 2014-10-01 to 2020-12-31, we derived the global 3-D magnetic
 478 field structure of the Martian induced magnetosphere. Our findings can be summarized as
 479 follows:

- 480 (1) The magnetic field structure around Mars is basically controlled by solar wind flow and
 481 IMF orientation, and the resulting morphology of the Martian magnetosphere conforms
 482 to the typical draping picture of an induced magnetosphere: a pair of tail lobes that is
 483 induced in the wake.

- 484 (2) The draped field lines from both flanks of the \pm E-hemisphere are directed towards the
 485 magnetic equatorial plane, making the field lines look like they are “sinking” toward the
 486 wake. These “sinking” field lines could be driven by a downstream convergence of solar
 487 wind flow to the wake plasma cavity [Rong et al., 2014; Dubinin et al., 2019]. The field
 488 lines “sinking” from the +E-hemisphere are dominant in Martian tail because they can
 489 extend down to $\sim Z_{MSE} = -1 R_m$. The “sinking” field lines from the –E-hemisphere are
 490 more stretched and even “pinched” towards the central plasma sheet. The E-asymmetry
 491 of the “sinking fields” is consistent with previous studies on the field structure of Mars
 492 magnetotail [Dubinin et al., 2019, 2021] and also the Venusian magnetotail [Rong et al.,
 493 2014]. However, the E-asymmetry of “sinking fields” disappears outside the MPB,
 494 which indicates that asymmetry might arise due to the interaction of solar wind with the
 495 low-altitude atmosphere of Mars.
- 496 (3) The tail current sheet also shows an evident E-asymmetry corresponding to the E-
 497 asymmetry of draped field lines. The current sheet is thicker in the +E-hemisphere and
 498 thinner in the –E-hemisphere, and the tailward Ampere force $\bar{J} \times \bar{B}$ at the current sheet
 499 center, which is stronger near the flank of +E-hemisphere, is attenuated as it moves
 500 towards the –E-hemisphere. Thus, the tailward plasma flow can be accelerated to higher
 501 speeds by $\bar{J} \times \bar{B}$ near the flank of the +E-hemisphere. The much thinner current sheet
 502 and the sunward $\bar{J} \times \bar{B}$ at the flank of the –E-hemisphere may indicate that magnetic
 503 reconnection occurs preferentially there and explain the sunward ions observed there as
 504 well [Harada et al., 2015].
- 505 (4) Possible effects of IMF B_x , P_{dy} , and planetary rotation on the magnetic field structure
 506 are checked respectively. We find that a kink-like field structure appears at the boundary
 507 layer of the Martian magnetosphere under the presence of a significant IMF B_x
 508 component. While the global induced magnetic field around Mars is enhanced due to the
 509 compression of higher P_{dy} , the draped field lines in the tail flare less in such conditions.
 510 However, variations in the crustal field that are caused by planetary rotation do not seem
 511 to affect or modulate the configuration of tail current sheet significantly.

512 The E-asymmetry of the field structure has been observed in Venusian and Titan
 513 magnetotails [e. g. Saunders and Russell, 1986; Zhang et al., 2010; Du et al., 2013; Rong et al.,

514 2014; Chai et al., 2016; Simon et al., 2006]; thus, it appears to be a ubiquitous phenomenon of
515 induced magnetospheres. However, the physical mechanism responsible for E-asymmetry is still
516 unclear. Previous studies on Venus demonstrated that E-asymmetry of the B_y component has
517 appeared at low altitude around the terminator [Du et al., 2013] and can extend to the distant tail
518 [Saunders and Russell, 1986]. This asymmetry can be reproduced in hybrid and multifluid
519 magnetohydrodynamic simulations but not in single-fluid ones [e.g., Zhang et al., 2010;
520 Du et al., 2013, and references therein; Jarvinen et al., 2013]. Thus, it seems that E-asymmetry
521 could be associated with particle kinetic effects. Similar to research on Venus, our study on Mars
522 also demonstrates that the appearance of the $-B_y$ component starts at a low-altitude around the
523 terminator of the $-E$ -hemisphere (see Figures 2d and 2h). Recent observations by MAVEN
524 showed that there is a trail of O^+ , extended from nightside ionosphere, in the $-E$ -hemisphere
525 [Dubinin et al., 2019]. Thus, the interaction of the O^+ trail with the draped IMF would seem to
526 result in a kinetic effect that “drags” the draped field lines, making them more stretched out, as
527 well as resulting in a weaker B_y and signature of $-B_y$ in the hemisphere. Dubinin et al. [2019,
528 2021] suggested that ionospheric plasma is extracted and accelerates toward the $+E$ direction by
529 the pick-up effect of solar wind, which in turn produces an $-E$ -directing recoil effect to the
530 ionosphere, forming an ion trail in the $-E$ hemisphere. However, this recoil force is not well
531 identified. Additionally, it is also unclear why the appearance of $-B_y$ starts at a low-altitude
532 around the terminator of the $-E$ -hemisphere instead of the $+E$ -hemisphere. It might be that the
533 draped IMF penetrates more easily into the ionosphere when in the $-E$ -hemisphere (as opposed
534 to the $+E$ -hemisphere) under the motional solar wind electric field, so that the signature of $-B_y$
535 tends to appear under those conditions. A combination of future simulations may help unravel the
536 real mechanism of this E-asymmetry.

537 An important feature of E-asymmetry is a loop field structure over the pole of $-E$ -
538 hemisphere (Figure 6), which has been interpreted as the product of magnetic reconnection
539 [Dubinin et al., 2019, 2021]. Given the explosive process of magnetic reconnection with a
540 transient timescale, however, it is hard to believe that an average-yielded loop field structure,
541 seen as a temporally static structure, is the product of magnetic reconnection. We suggest instead
542 that the loop structure is induced by the inhomogeneous distribution of current density, and there
543 should be stronger current density flowing $+Z_{MSE}$ direction embedded in the loop. The pattern of

544 the global Martian magnetospheric current derived by Ramstad et al. [2020] supports our
545 interpretation.

546 Our study shows that the rotation of crustal field cannot affect the configuration of the tail
547 current sheet significantly, which seems inconsistent with DiBraccio et al. [2018]. They argued
548 that the current sheet could be twisted by open field lines owing to the reconnection between the
549 IMF and crustal fields, a twist that could be more significant when the strongest crustal fields are
550 on the noon. But the study by DiBraccio et al. was performed using MSO instead of MSE
551 coordinates, which we favor here. We will address reasons for the discrepancy in a future study.

552 Finally, we also expect that future studies combining multipoint observations from China's
553 TIANWEN-1 [Wan et al., 2020], MAVEN, and Mars Express [Barabash et al. 2006] might offer
554 better opportunities to study the Martian magnetosphere and its response to solar wind variation
555 and crustal field rotation.

556

557 **Data Availability Statement**

558 All MAVEN data used in this paper are available from NASA's Planetary Data System.
559 MAG data can be found at <https://pds-ppi.igpp.ucla.edu/mission/MAVEN/MAVEN/MAG>.
560 SWIA data can be found at <https://pds-ppi.igpp.ucla.edu/mission/MAVEN/MAVEN/SWIA>.
561 SWEA data can be found at <https://pds-ppi.igpp.ucla.edu/mission/MAVEN/MAVEN/SWEA>.

562

563 **Acknowledgments**

564 We would like to thank the entire MAVEN team and instrument leads for access to data and
565 support. Special thanks to Jasper Halekas, David Mitchell and John E. P. Connerney for their
566 contributions regarding the availability of SWIA, SWEA, and MAG data, respectively. This
567 work is supported by the National Natural Science Foundation of China (Grant Nos. 41922031,
568 41774188), the Strategic Priority Research Program of Chinese Academy of Sciences (Grant No.
569 XDA17010201), the Key Research Program of Chinese Academy of Sciences (Grant No. ZDBS-
570 SSW-TLC00103), and the Key Research Program of the Institute of Geology & Geophysics,
571 CAS (Grant No. IGGCAS- 201904, IGGCAS- 202102). Chi Zhang is supported by the China
572 Scholarship Council (Student No. 202104910297). We also thank Jun Zhong and Chongjing
573 Yuan for helpful suggestions, and Fang Qian for her encouragement.

574 **References**

- 575 Acuña, M. H., Connerney, J. E. P., Ness, N. F., Lin, R. P., Mitchell, D., Carlson, C.W., et al.
 576 (1999). Global distribution of crustal magnetism discovered by Mars Global Surveyor
 577 MAG/ER experiment. *Science*, 284, 790–793. <https://doi.org/10.1126/science.284.5415.790>
 578 Acuña, M.H., et al., 1998. Magnetic field and plasma observations at Mars: initial results of the
 579 Mars Global Surveyor mission. *Science*, 279, 1676–1680.
- 580 Barabash, S., et al. (2006), The Analyzer of Space Plasma and Energetic Atoms (ASPERA-3) for
 581 the Mars Express mission, *Space Sci. Rev.*, 126, 113.
- 582 Barabash, S., Fedorov, A., Lundin, R., & Sauvaud, J.-A. (2007). Martian Atmospheric Erosion
 583 Rates. *Science*, 315(5811), 501–503.
- 584 Chai, L., Wan, W., Wei, Y., Zhang, T., Exner, W., Fraenz, M., ... & Zhong, J. (2019). The
 585 induced global looping magnetic field on Mars. *The Astrophysical Journal Letters*, 871(2),
 586 L27.
- 587 Chai, L., Wei, Y., Wan, W., Zhang, T., Rong, Z., Fraenz, M., ... & Barabash, S. (2016). An
 588 induced global magnetic field looping around the magnetotail of Venus. *Journal of*
 589 *Geophysical Research: Space Physics*, 121(1), 688-698.
- 590 Connerney, J. E. P., Acuña, M. H., Ness, N. F., Kletetschka, G., Mitchell, D. L., Lin, R. P., &
 591 Rème, H. (2005). Tectonic implications of Mars crustal magnetism. *Proceedings of the*
 592 *National Academy of Sciences of the United States of America*, 102(42), 14970 – 14975.
 593 <https://doi.org/10.1073/pnas.0507469102>
- 594 Connerney, J., Espley, J., Lawton, P., Murphy, S., Odom, J., Oliverson, R., & Sheppard, D.
 595 (2015). The MAVEN magnetic field investigation. *Space Science Reviews*, 195, 257–291.
- 596 Delva, M., Volwerk, M., Jarvinen, R., & Bertucci, C. (2017). Asymmetries in the magnetosheath
 597 field draping on Venus' nightside. *Journal of Geophysical Research: Space Physics*, 122(10),
 598 10-396.
- 599 DiBraccio, G. A., Luhmann, J. G., Curry, S. M., Espley, J. R., Xu, S., Mitchell, D. L., et al.
 600 (2018). The twisted configuration of the Martian magnetotail: MAVEN observations.
 601 *Geophysical Research Letters*, 45, 4559–4568. <https://doi.org/10.1029/2018GL077251>
 602 Du, J., C. Wang, T. L. Zhang, and E. Kallio (2013), Asymmetries of the magnetic field line
 603 draping shape around Venus, *J. Geophys. Res. Space Physics*, 118, 6915–6920,
 604 doi:10.1002/2013JA019127
- 605 Dubinin, E., & Fraenz, M. (2015). Magnetotails of Mars and Venus. In A. Keiling, C. M. Jackman,
 606 & P. A. Delamere (Eds.), *Magnetotails in the solar system* (pp. 43–59). Hoboken, NJ: John
 607 Wiley. <https://doi.org/10.1002/9781118842324.ch3>
- 608 Dubinin, E., Fraenz, M., Fedorov, A., Lundin, R., Edberg, N., Duru, F., & Vaisberg, O. (2011).
 609 Ion Energization and Escape on Mars and Venus. *Space Science Reviews*, 162(1), 173–211.
- 610 Dubinin, E., Fraenz, M., Pätzold, M., McFadden, J., Halekas, J., DiBraccio, G., et al. (2017). The
 611 effect of solar wind variations on the escape of oxygen ions from Mars through different
 612 channels: MAVEN observations. *Journal of Geophysical Research: Space Physics*, 122,
 613 11,285–11,301. <https://doi.org/10.1002/2017JA024741>
- 614 Dubinin, E., Fränz, M., Modolo, R., Pätzold, M., Tellmann, S., Vaisberg, O., ... & Espley, J.
 615 (2021). Induced magnetic fields and plasma motions in the inner part of the Martian
 616 magnetosphere. *Journal of Geophysical Research: Space Physics*, 126(12), e2021JA029542.
- 617 Dubinin, E., Fränz, M., Pätzold, M., Woch, J., McFadden, J., Fan, K., ... & Zelenyi, L. (2020).
 618 Impact of Martian crustal magnetic field on the ion escape. *Journal of Geophysical*
 619 *Research: Space Physics*, 125(10), e2020JA028010.

- 620 Dubinin, E., Modolo, R., Fraenz, M., Päetzold, M., Woch, J., Chai, L., ... DiBraccio, G. (2019).
 621 The induced magnetosphere of Mars. Asymmetrical topology of the magnetic field lines.
 622 Geophysical Research Letters, 46(22), 12722–12730.
- 623 Fang, X., Liemohn, M. W., Nagy, A. F., Luhmann, J. G., & Ma, Y. (2010). Escape probability of
 624 Martian atmospheric ions: Controlling effects of the electromagnetic fields. Journal of
 625 Geophysical Research: Space Physics, 115(A4).
- 626 Fang, X., Liemohn, M. W., Nagy, A. F., Luhmann, J. G., & Ma, Y. (2010). On the effect of the
 627 Martian crustal magnetic field on atmospheric erosion. *Icarus*, 206(1), 130-138.
- 628 Fedorov, A., Budnik, E., Sauvaud, J. A., Mazelle, C., Barabash, S., Lundin, R., ... Yamauchi, M.
 629 (2006). Structure of the martian wake. *Icarus*, 182(2), 329–336.
- 630 Futaana, Y. , Wieser, G. S. , Barabash, S. , & Luhmann, J. G. . (2017). Solar wind interaction and
 631 impact on the venus atmosphere. *Space Science Reviews*.
- 632 Gao, J.W., Rong, Z.J., Klinger Lucy, Li, X.Z., Liu, D., Wei, Y. (2021). A spherical harmonic
 633 Martian crustal magnetic field model combining data sets of MAVEN and MGS, *Earth and*
 634 *Space Science*, doi: 10.1029/2021EA001860.
- 635 Halekas, J. S., D. A. Brain, R. J. Lillis, M. O. Fillingim, D. L. Mitchell, and R. P. Lin (2006),
 636 Current sheets at low altitudes in the Martian magnetotail, *Geophys. Res. Lett.*, 33, L13101,
 637 doi:10.1029/2006GL026229.
- 638 Halekas, J. S., E. R. Taylor, G. Dalton, G. Johnson, D. W. Curtis, J. P. McFadden, D. L. Mitchell,
 639 R. P. Lin, and B. M. Jakosky (2013), The solar wind ion analyzer for MAVEN, *Space Sci.*
 640 *Rev.*, doi:10.1007/s11214-013-0029-z.
- 641 Harada, Y., Halekas, J. S., McFadden, J. P., Mitchell, D. L., Mazelle, C., Connerney, J. E. P., ...
 642 & Jakosky, B. M. (2015). Marsward and tailward ions in the near - Mars magnetotail:
 643 MAVEN observations. *Geophysical Research Letters*, 42(21), 8925-8932.
- 644 Harris, E. G. (1962), On a plasma sheet separating regions of oppositely directed magnetic field,
 645 *Nuovo Cimento*, 23, 115–121, doi:10.1007/BF02733547.
- 646 Inui, S., Seki, K., Sakai, S., Brain, D. A., Hara, T., McFadden, J. P., et al. (2019). Statistical
 647 study of heavy ion outflows from Mars observed in the Martian - induced magnetotail by
 648 MAVEN. *Journal of Geophysical Research: Space Physics*, 124, 5482–5497.
 649 <https://doi.org/10.1029/2018JA026452>
- 650 Jakosky, B. M., et al. (2015), The Mars Atmosphere and Volatile Evolution (MAVEN) mission,
 651 *Space Sci. Rev.*, doi:10.1007/s11214-015-0139-x.
- 652 Jarvinen, R., E. Kallio, and S. Dyadechkin (2013), Hemispheric asymmetries of the Venus
 653 plasma environment, *J. Geophys. Res. Space Physics*, 118, 4551–4563,
 654 doi:10.1002/jgra.50387.
- 655 Jarvinen, R., Kallio, E., Dyadechkin, S., Janhunen, P., & Sillanpää, I. (2010). Widely different
 656 characteristics of oxygen and hydrogen ion escape from Venus. *Geophysical research letters*,
 657 37(16).
- 658 Liu, D., Rong, Z., Gao, J., He, J., Klinger, L., Dunlop, M. W., ... & Wei, Y. (2021). Statistical
 659 Properties of Solar Wind Upstream of Mars: MAVEN Observations. *The Astrophysical*
 660 *Journal*, 911(2), 113.
- 661 Luhmann, J. G., Dong, C., Ma, Y., Curry, S. M., Mitchell, D., Espley, J., ... & Mazelle, C. (2015).
 662 Implications of MAVEN Mars near-wake measurements and models. *Geophysical Research*
 663 *Letters*, 42(21), 9087-9094.
- 664 Luhmann, J. G., S. A. Ledvina, and C. T. Russell (2004), Induced magnetospheres, *Adv. Space*
 665 *Res.*, 33, 1905–1912.

- 666 Lundin, R. (2011). Ion acceleration and outflow from Mars and Venus: An overview. The
667 plasma environment of Venus, Mars, and Titan, 309-334.
- 668 Ma, Y., Nagy, A. F., Hansen, K. C., DeZeeuw, D. L., Gombosi, T. I., & Powell, K. (2002).
669 Three-dimensional multispecies MHD studies of the solar wind interaction with Mars in the
670 presence of crustal fields. *Journal of Geophysical Research*, 107(A10), 1282–1289.
- 671 McComas, D. J., H. E. Spence, C. T. Russell, and M. A. Saunders (1986), The average magnetic
672 field draping and consistent plasma properties in the Venus magnetotail, *J. Geophys. Res.*,
673 91, 7939–7953, doi:10.1029/JA091iA07p07939.
- 674 Mitchell, D., Mazelle, C., Sauvaud, J.-A., Thocaven, J.-J., Rouzaud, J., Fedorov, A., et al. (2016).
675 The MAVEN solar wind electron analyzer. *Space Science Reviews*, 200(1-4), 495–528.
- 676 Nilsson, H., Carlsson, E., Brain, D. A., Yamauchi, M., Holmström, M., Barabash, S., ... &
677 Futaana, Y. (2010). Ion escape from Mars as a function of solar wind conditions: A
678 statistical study. *Icarus*, 206(1), 40-49.
- 679 Nilsson, H., Edberg, N. J. T., Stenberg, G., Barabash, S., Holmström, M., Futaana, Y., ...
680 Fedorov, A. (2011). Heavy ion escape from Mars, influence from solar wind conditions and
681 crustal magnetic fields. *Icarus*, 215(2), 475–484.
- 682 Nilsson, H., Zhang, Q., Wieser, G. S., Holmström, M., Barabash, S., Futaana, Y., ... Wieser, M.
683 (2021). Solar cycle variation of ion escape from Mars. *Icarus*, 114610.
- 684 Ramstad, R., Barabash, S., Futaana, Y., Nilsson, H., & Holmström, M. (2016). Effects of the
685 crustal magnetic fields on the Martian atmospheric ion escape rate. *Geophysical Research*
686 *Letters*, 43(20), 10-574.
- 687 Ramstad, R., Barabash, S., Futaana, Y., Nilsson, H., Wang, X. D., & Holmström, M. (2015). The
688 Martian atmospheric ion escape rate dependence on solar wind and solar EUV conditions: 1.
689 Seven years of Mars Express observations. *Journal of Geophysical Research: Planets*,
690 120(7), 1298-1309.
- 691 Ramstad, R., Brain, D. A., Dong, Y., Espley, J., Halekas, J., & Jakosky, B. (2020). The global
692 current systems of the Martian induced magnetosphere. *Nature Astronomy*, 4(10), 979-985.
- 693 Romanelli, N., Bertucci, C., Gómez, D., & Mazelle, C. (2015). Dependence of the location of the
694 Martian magnetic lobes on the interplanetary magnetic field direction: Observations from
695 Mars Global Surveyor. *Journal of Geophysical Research: Space Physics*, 120(9), 7737-7747.
- 696 Rong, Z. J., G. Stenberg, Y. Wei, L. H. Chai, Y. Futaana, S. Barabash, W. X. Wan, and C. Shen
697 (2016), Is the flow-aligned component of IMF really able to impact the magnetic field
698 structure of Venusian magnetotail? *J. Geophys. Res. Space Physics*, 121, 10,978–10,993,
699 doi:10.1002/2016JA022413.
- 700 Rong, Z. J., S. Barabash, Y. Futaana, G. Stenberg, T. L. Zhang, W. X. Wan, Y. Wei, X.-D. Wang,
701 L. H. Chai, and J. Zhong (2014), Morphology of magnetic field in near-Venus magnetotail:
702 Venus express observations, *J. Geophys. Res. Space Physics*, 119, 8838–8847,
703 doi:10.1002/2014JA020461.
- 704 Saunders, M. A., and C. T. Russell (1986), Average dimension and magnetic structure of the
705 distant Venus magnetotail, *J. Geophys. Res.*, 91, 5589 – 5604,
706 doi:10.1029/JA091iA05p05589.
- 707 Shen, C., X. Li, M. Dunlop, Q. Q. Shi, Z. X. Liu, E. Lucek, and Z. Q. Chen (2007), Magnetic
708 field rotation analysis and the applications, *J. Geophys. Res.*, 112, A06211,
709 doi:10.1029/2005JA011584.

- 710 Simon, S. , Boesswetter, A. , Bagdonat, T. , Motschmann, U. , & Glassmeier, K. H. . (2006).
711 Plasma environment of titan: a 3-d hybrid simulation study. *Annales Geophysicae*, 24(2006),
712 1113-1135.
- 713 Sonnerup, B. U. Ö., & Scheible, M. (1998). Minimum and maximum variance analysis. In G.
714 Paschmann, & P. W. Daly (Eds.), chap. 8, *Analysis Methods for Multi - Spacecraft Data*,
715 *ISSI Sci. Rep. no. SR - 001* (pp. 185–220). Noordwijk, Netherlands: European Space
716 Agency.
- 717 Titov, D. V., Svedhem, H., Koschny, D., Hoofs, R., Barabash, S., Bertaux, J. L., ... & Clochet, A.
718 (2006). Venus Express science planning. *Planetary and Space Science*, 54(13-14), 1279-
719 1297.
- 720 Trotignon, J. G., Mazelle, C., Bertucci, C., & Acuña, M. H. (2006). Martian shock and magnetic
721 pile-up boundary positions and shapes determined from the Phobos 2 and Mars Global
722 Surveyor data sets. *Planetary and Space Science*, 54(4), 357–369.
- 723 Wan, W., Wang, C., Li, C., Wei, Y., & Liu, J. (2020). The payloads of planetary physics
724 research onboard China's First Mars Mission (Tianwen-1). *Earth and Planetary Physics*,
725 4(4), 331–332.
- 726 Xu, S., Mitchell, D. L., Weber, T., Brain, D. A., Luhmann, J. G., Dong, C., et al. (2020).
727 Characterizing Mars's magnetotail topology with respect to the upstream interplanetary
728 magnetic fields. *Journal of Geophysical Research: Space Physics*, 125, e2019JA027755.
729 <https://doi.org/10.1029/2019JA027755>
- 730 Yeroshenko, Y., Riedler, W., Schwingenschuh, K., Luhmann, J. G., Ong, M., & Russell, C. T.
731 (1990). The magnetotail of Mars: Phobos observation. *Geophysical Research Letters*, 17,
732 885–888. <https://doi.org/10.1029/GL017i006p00885>
- 733 Zhang, C., Rong, Z. J., et al. (2021). MAVEN Observations of Periodic Low-altitude Plasma
734 Clouds at Mars. *The Astrophysical Journal Letters*, 922, L33. [https://doi.org/10.3847/2041-
735 8213/ac3a7d](https://doi.org/10.3847/2041-8213/ac3a7d)
- 736 Zhang, T. L., Schwingenschuh, K., Russell, C. T., Luhmann, J. G., Rosenbauer, H., Verigin, M.
737 I., & Kotova, G. (1994). The flaring of the Martian magnetotail observed by the Phobos 2
738 spacecraft. *Geophysical research letters*, 21(12), 1121-1124.
- 739 Zhang, T., Baumjohann, W., Du, J., Nakamura, R., Jarvinen, R., Kallio, E., et al. (2010).
740 Hemispheric asymmetry of the magnetic field wrapping pattern in the Venusian magnetotail.
741 *Geophysical Research Letters*, 37, L14202, <https://doi.org/10.1029/2010GL044020>.
742